

NGTS-14Ab: a Neptune-sized transiting planet in the desert[★]

A. M. S. Smith¹, J. S. Acton², D. R. Anderson^{3,4}, D. J. Armstrong^{3,4}, D. Bayliss^{3,4}, C. Belardi², F. Bouchy⁵, R. Brahm^{6,7}, J. T. Briegal⁸, E. M. Bryant^{3,4}, M. R. Burleigh², J. Cabrera¹, A. Chaushev⁹, B. F. Cooke^{3,4}, J. C. Costes¹⁰, Sz. Csizmadia¹, Ph. Eigmüller¹, A. Erikson¹, S. Gill^{3,4}, E. Gillen^{8,11,***}, M. R. Goad², M. N. Günther^{12,***}, B. A. Henderson², A. Hogan², A. Jordán^{6,7}, M. Lendl⁵, J. McCormac^{3,4}, M. Moyano¹³, L. D. Nielsen⁵, H. Rauer^{1,9,14}, L. Raynard², R. H. Tilbrook², O. Turner⁵, S. Udry⁵, J. I. Vines¹⁵, C. A. Watson¹⁰, R. G. West^{3,4}, and P. J. Wheatley^{3,4}

¹ Institute of Planetary Research, German Aerospace Center, Rutherfordstrasse 2, 12489 Berlin, Germany
e-mail: alexis.smith@dlr.de

² School of Physics and Astronomy, University of Leicester, LE1 7RH, UK

³ Centre for Exoplanets and Habitability, University of Warwick, Gibbet Hill Road, Coventry CV4 7AL, UK

⁴ Department of Physics, University of Warwick, Gibbet Hill Road, Coventry CV4 7AL, UK

⁵ Observatoire de Genève, Université de Genève, 51 Ch. des Maillettes, 1290 Sauverny, Switzerland

⁶ Facultad de Ingeniería y Ciencias, Universidad Adolfo Ibáñez, Av. Diagonal las Torres 2640, Peñalolén, Santiago, Chile

⁷ Millennium Institute for Astrophysics, Santiago, Chile

⁸ Astrophysics Group, Cavendish Laboratory, J.J. Thomson Avenue, Cambridge CB3 0HE, UK

⁹ Center for Astronomy and Astrophysics, TU Berlin, Hardenbergstr. 36, 10623 Berlin, Germany

¹⁰ Astrophysics Research Centre, School of Mathematics and Physics, Queen's University Belfast, BT7 1NN Belfast, UK

¹¹ Astronomy Unit, Queen Mary University of London, Mile End Road, London E1 4NS, UK

¹² Department of Physics, and Kavli Institute for Astrophysics and Space Research, Massachusetts Institute of Technology, 77 Mass. Ave, Cambridge, MA 02139, USA

¹³ Instituto de Astronomía, Universidad Católica del Norte, Angamos 0610, 1270709 Antofagasta, Chile

¹⁴ Institute of Geological Sciences, FU Berlin, Malteserstr. 74-100, 12249 Berlin, Germany

¹⁵ Departamento de Astronomía, Universidad de Chile, Casilla 36-D, Santiago, Chile

Received 19 October 2020 / Accepted 5 January 2020

ABSTRACT

Context. The sub-Jovian, or Neptunian, desert is a previously identified region of parameter space where there is a relative dearth of intermediate-mass planets with short orbital periods.

Aims. We present the discovery of a new transiting planetary system within the Neptunian desert, NGTS-14.

Methods. Transits of NGTS-14Ab were discovered in photometry from the Next Generation Transit Survey (NGTS). Follow-up transit photometry was conducted from several ground-based facilities, as well as extracted from TESS full-frame images. We combine radial velocities from the HARPS spectrograph with the photometry in a global analysis to determine the system parameters.

Results. NGTS-14Ab has a radius that is about 30 per cent larger than that of Neptune ($0.444 \pm 0.030 R_{\text{Jup}}$) and is around 70 per cent more massive than Neptune ($0.092 \pm 0.012 M_{\text{Jup}}$). It transits the main-sequence K1 star, NGTS-14A, with a period of 3.54 days, just far away enough to have maintained at least some of its primordial atmosphere. We have also identified a possible long-period stellar mass companion to the system, NGTS-14B, and we investigate the binarity of exoplanet host stars inside and outside the Neptunian desert using *Gaia*.

Key words. planetary systems – planets and satellites: detection – planets and satellites: individual: NGTS-14Ab – binaries: general

1. Introduction

The first generation of wide-field transit surveys, the most prolific of which were SuperWASP (Pollacco et al. 2006) and HAT-Net (Bakos et al. 2002), unveiled the rich diversity of hot Jupiters. These planets, although intrinsically rare, have been discovered in numbers large enough to enable statistical population analyses, such as those investigating inflation (e.g. Thorngren & Fortney 2018; Sestovic et al. 2018). Transiting hot

Jupiters also remain the best studied individual planetary systems, with characterisation observations, such as atmospheric transmission spectroscopy, pioneered on these objects (e.g. Sing et al. 2016).

The *Kepler* (Borucki et al. 2010) and K2 (Howell et al. 2014) missions as well as the ongoing TESS (Transiting Exoplanet Survey Satellite; Ricker et al. 2015) mission have subsequently revealed a large population of small (less than 2–3 Earth radii), short-period planets. In between these two populations, however, lies a relatively unpopulated region of parameter space, often referred to as the sub-Jovian, or Neptunian, desert (Szabó & Kiss 2011; Mazeh et al. 2016).

The Next Generation Transit Survey (NGTS; Wheatley et al. 2018) consists of 12 independent 0.2-m telescopes, each

* Full Table 2 is only available at the CDS via anonymous ftp to cdsarc.u-strasbg.fr (130.79.128.5) or via <http://cdsarc.u-strasbg.fr/viz-bin/cat/J/A+A/646/A183>

** Winton Fellow.

*** Juan Carlos Torres Fellow.

Table 1. Catalogue information for NGTS-14A and NGTS-14B.

Positions & proper motions	NGTS-14A	NGTS-14B	Source
RA (J2015.5)	21h54m04.20s	21h54m03.89s	<i>Gaia</i>
Dec (J2015.5)	−38° 22′ 38″.71	−38° 22′ 38″.55	<i>Gaia</i>
pmRA (mas yr ^{−1})	−23.662 ± 0.042	−23.282 ± 0.191	<i>Gaia</i>
pmDec (mas yr ^{−1})	5.488 ± 0.034	6.602 ± 0.192	<i>Gaia</i>
parallax (mas)	3.076 ± 0.034	3.088 ± 0.176	<i>Gaia</i>
Projected separation from NGTS-14A	–	3″.59016 ± 0″.00015	<i>Gaia</i>
Distance from Earth (pc) ^(†)	316.7 ± 4.8	316 ± 18	
Magnitudes			
<i>B</i> (Johnson)	14.093 ± 0.055	–	APASS
<i>V</i> (Johnson)	13.237 ± 0.078	–	APASS
<i>G</i> (<i>Gaia</i>)	13.0986 ± 0.0006	17.197 ± 0.004	<i>Gaia</i>
<i>BP</i> (<i>Gaia</i>)	13.5448 ± 0.0014	18.147 ± 0.060	<i>Gaia</i>
<i>RP</i> (<i>Gaia</i>)	12.5095 ± 0.0008	15.947 ± 0.020	<i>Gaia</i>
<i>g</i> ' (Sloan)	13.607 ± 0.084	–	APASS
<i>r</i> ' (Sloan)	12.989 ± 0.054	–	APASS
<i>i</i> ' (Sloan)	12.751 ± 0.056	–	APASS
TESS	12.5638 ± 0.006	16.211 ± 0.014	TESS
<i>J</i>	11.813 ± 0.029	≥12.431 (2 σ limit)	2MASS
<i>H</i>	11.386 ± 0.037	≥11.859 (2 σ limit)	2MASS
<i>K</i>	11.305 ± 0.027	13.474 ± 0.070	2MASS
<i>W1</i>	11.148 ± 0.022	–	WISE
<i>W2</i>	11.212 ± 0.020	–	WISE
<i>W3</i>	11.334 ± 0.166	–	WISE
Spectral type	K1V	M3V	Sect. 2
Additional identifiers			
<i>Gaia</i> DR2	6585082036193768832	6585082036193769088	
2MASS J	21540423-3822388	21540393-3822386	
TIC	197643976	197641898	

Notes. *Gaia*: *Gaia* DR2 (Gaia Collaboration 2016, 2018) APASS: AAVSO Photometric all-sky survey DR9 (Henden et al. 2016) 2MASS: The Two Micron All Sky Survey (Skrutskie et al. 2006) WISE: Wide-field Infrared Survey Explorer (Cutri et al. 2014) ^(†)Calculated from *Gaia* DR2 parallax, incorporating the systematic offset of Stassun & Torres (2018).

equipped with a red-sensitive 2k × 2k charge-coupled device (CCD) covering eight square degrees. The survey is optimised for detecting short-period planets transiting K-dwarf stars, with the goal of detecting Neptune-sized planets. One of the main drivers for the extremely high-precision photometry achieved by NGTS is the telescope guiding, which uses DONUTS (McCormac et al. 2013) to ensure sub-pixel pointing precision throughout the duration of an observing season. This has allowed the detection of significantly shallower transits than previously achieved from the ground, as well as the discovery of planets in the Neptunian desert, such as NGTS-4b (West et al. 2019).

In this paper, we report the discovery from NGTS of a transiting planet slightly larger than Neptune orbiting the early K-dwarf NGTS-14A. In Sect. 2, we present the host star and show that it probably has a bound long-period M-dwarf companion. In Sect. 3, we present our observations of the system with both NGTS and other facilities. In Sect. 4, we characterise the host star, and, in Sect. 5, we perform a joint analysis of the transit photometry and radial velocities (RVs) to determine the system parameters. Finally, we discuss NGTS-14 in the context of the Neptunian desert in Sect. 6, and summarise our findings in Sect. 7.

2. NGTS-14B

We list in Table 1 the *Gaia* positions, proper motions, and parallaxes (Gaia Collaboration 2018) for both NGTS-14A and NGTS-14B, the latter a fainter star that lies just 3.59 arcsec from the former (see Fig. 1). The parallaxes of the two objects are identical to much less than 1 σ significance, and the proper motions in the right ascension (RA) direction are compatible at the 2 σ level. We note, however, that in the declination (dec) direction, the proper motions differ from each other with a significance of 5.7 σ . Nevertheless, we conclude that these two stars are co-moving and are likely to be gravitationally bound.

As a test of the statistical significance of finding a companion with similar parallax and proper motions close to our target, we searched the *Gaia* DR2 catalogue for all stars lying within 5° of NGTS-14A¹ and whose proper motions and parallaxes match those of NGTS-14A to within 6 σ . This search of an area 2.5 × 10⁷ times larger than the area defined by a radius equal to the separation between target and putative companion returned exactly 100 results, excluding NGTS-14A itself. This

¹ *Gaia* DR2 reports a total of 4.78 × 10⁵ sources within 5° of NGTS-14A.

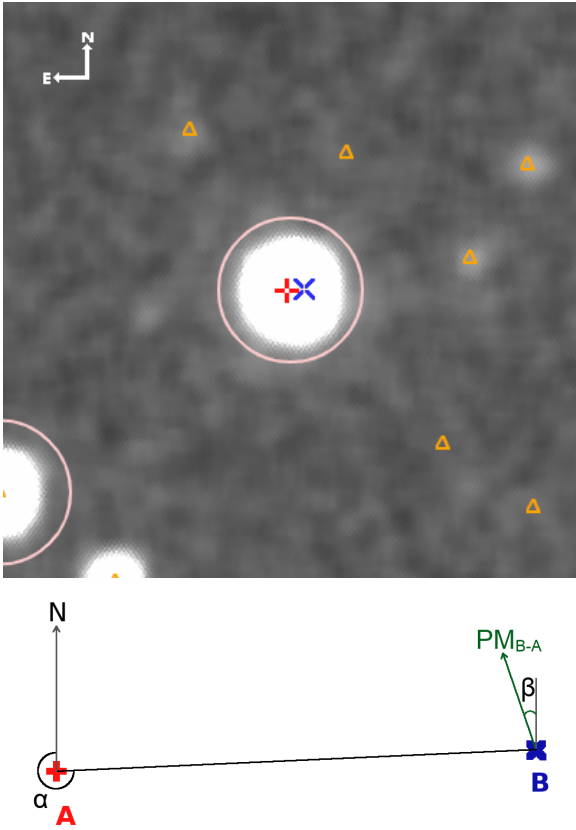


Fig. 1. Sky positions of NGTS-14A and NGTS-14B. *Upper panel:* NGTS deep stacked image ($2' \times 2'$) centred on NGTS-14A. The *Gaia* positions of NGTS-14A and NGTS-14B are indicated with a red '+' and a blue 'x', respectively. The pink circle indicates the NGTS photometric aperture, which has a radius of 3 pixels ($15''$). Other *Gaia* sources are marked with orange triangles. North is up, and east is to the left. *Lower panel:* sketch of NGTS-14 showing the separation of NGTS-14A and NGTS-14B, which are represented by the same symbols as in the *upper panel*. NGTS-14B lies on a bearing of $\alpha = 267.49$ degrees from NGTS-14A. The direction of the relative proper motion of NGTS-14B with respect to NGTS-14A is indicated with the green arrow. The bearing of this proper motion vector is $\beta = 18.8 \pm 9.5$ degrees, and its magnitude is 1.18 ± 0.20 mas yr^{-1} .

implies that the chance of finding such an object within $3''.6$ is around 4×10^{-6} .

At a distance of 316.7 ± 4.8 pc, the projected separation of the two stars implies a physical separation of 1137 ± 17 au. If the two objects are gravitationally bound, this sets a lower limit to the binary orbital period of around 40 000 yr, assuming a circular orbit. For a moderately eccentric orbit (0.6), this lower limit is reduced to around 20 000 yr, which is the orbital period obtained if we assume that we are observing NGTS-14B at apastron. We note that the physical separation implied here is an order of magnitude smaller than the widest binary that can survive for ~ 10 Gyr in the Solar neighbourhood (Jiang & Tremaine 2010).

We also note that, at a distance of around 320 pc, the apparent discrepancy in proper motions in the dec direction (1.1 ± 0.2 mas yr^{-1}) corresponds to a physical velocity of around 1.5 km s^{-1} , which could be easily explained by the orbital motion of the secondary with respect to the primary. We searched the Digitized Sky Survey for archival imaging, but we found no images with sufficient angular resolution to resolve the two sources. An RV measurement of NGTS-14B would provide further evidence of whether or not the two stars are really a

binary pair, but NGTS-14B is too faint to be observed with CORALIE or the High Accuracy Radial velocity Planet Searcher (HARPS; see Sect. 3.3).

The existence of such binary companions to planet host stars is interesting since, even at these very large separations, a binary companion may influence the evolution of the planet. For instance, long-period outer companions can act to maintain a non-zero planetary orbital eccentricity, even for short-period planets whose orbits would otherwise be rapidly circularised through tidal interactions with the host star (e.g. Wu & Murray 2003).

NGTS-14B is 4.098 ± 0.004 magnitudes fainter than NGTS-14A in the *G*-band and 2.17 ± 0.08 magnitudes fainter in the *K*-band. The spectral type of NGTS-14A is estimated to be K1V, based on the effective temperature derived from spectral analysis and the tabulation of Pecaut & Mamajek (2013)².

Based on the absolute *G*-band magnitudes in the aforementioned table, if NGTS-14A has a spectral type of K1V, then NGTS-14B is probably an M2.5V star. Alternatively, using the (*G*-*K*) colour, the best matching spectral types (according to the aforementioned table) are K1.5V and M3.5V for NGTS-14A and NGTS-14B, respectively. We adopted spectral types of K1V and M3V for the two stars and accounted for the flux contamination of NGTS-14B in our light curves (Sect. 5.1).

3. Observations

3.1. NGTS photometry

NGTS-14A lies in one of the fields that was observed by NGTS for around eight months, beginning with the start of routine science operations in 2016 April. In all, a total of 220 829 observations of this field were made using a single NGTS telescope between 2016 April 21 and 2016 December 22. Each image has an exposure time of 10 s and a typical cadence of 13 s. The data were reduced using the NGTS pipeline (Wheatley et al. 2018), which comprises standard bias subtraction and flat-field correction, followed by aperture photometry based on the CASUtools³ software package. Finally, systematic effects in the light curves were removed using the SYSREM algorithm (Tamuz et al. 2005).

The NGTS light curves were searched for period transit-like signals using our implementation of the box-fitting least-squares (BLS) algorithm (Kovács et al. 2002). In the case of NGTS-14A, a signal consistent with a transiting exoplanet was detected, with a periodicity of around 3.5 days. After passing several vetting checks designed to eliminate false positives, such as eclipsing binaries and blended systems (e.g. Günther et al. 2017), we initiated follow-up observations to confirm the planetary nature of the system and to better characterise it. We also note that this system received a high planetary probability of 0.97 from a neural network trained to distinguish between transiting planetary systems and false positives in NGTS data (Chaushev et al. 2019).

3.2. Follow-up photometry

We used several larger aperture telescopes, as well as multiple NGTS telescopes, to perform follow-up transit observations. The motivation of these observations was to confirm the transit, increase the signal-to-noise of our transit photometry to improve

² http://www.pas.rochester.edu/~emamajek/EEM_dwarf_UBVIJHK_colors_Teff.txt

³ <http://casu.ast.cam.ac.uk/surveys-projects/software-release>

the characterisation of the system, and improve our knowledge of the orbital ephemeris by extending the observational baseline.

3.2.1. SAAO 1-m

We observed a partial transit of NGTS-14Ab on the night of 2019 October 04 from the South African Astronomical Observatory (SAAO) in Sutherland, Northern Cape, using their 1-m telescope. The telescope was equipped with one of the Sutherland High-speed Optical Cameras (SHOC; specifically ‘SHOC’n’awe’). A description of the instrument can be found in [Coppejans et al. \(2013\)](#). The observations were conducted in I-band, in focus, with 4×4 binning of the CCD, and each of the 960 exposures had a duration of 20 s.

The data were bias- and flat-field-corrected via the standard procedure, using the SAFPHOT Python package (Chaushev & Raynard, in preparation). Differential photometry was also carried out using SAFPHOT, by first extracting aperture photometry for both the target and comparison stars using the SEP package ([Barbary 2016](#)). The sky background was measured and subtracted using the SEP background map, adopting box size and filter width parameters that minimised background residuals, measured across the frame after masking the stars. Three comparison stars were then utilised to perform differential photometry on the target, using a 3.4 pixel ($0''.57$) radius aperture that maximised the signal-to-noise.

3.2.2. EulerCam

A partial transit of NGTS-14Ab was observed on the night of 2019 August 08 with EulerCam on the 1.2-m Euler-Swiss telescope at La Silla Observatory in Chile. A total of 271 observations were made in a filter corresponding to the NGTS bandpass, each with an exposure time of 40 s, giving a cadence of around 52 s. A slight de-focus was applied during the observations. Standard data reduction and aperture photometry techniques were applied, using a photometric aperture radius of 19 pixels ($=4''.085$) and 17 comparison stars.

3.2.3. CHAT

Another partial transit of NGTS-14Ab was observed from the Chilean-Hungarian Automated Telescope (CHAT), a 0.7-m robotic telescope installed at Las Campanas Observatory in Chile. The observations were conducted on the night of 2019 November 08, using an i' filter. The cadence of the light curve is around 180 s, and 73 images were obtained that spanned airmass values between 1 and 2. The data were processed with a dedicated pipeline adapted from a set of routines to process photometric data of the LCOGT network (e.g. [Hartman et al. 2019](#); [Espinoza et al. 2019](#); [Jordán et al. 2019](#)).

3.2.4. NGTS multi-telescope observations

In addition to its survey mode, where each telescope observes a different field to maximise sky coverage, NGTS can also be operated in a mode where multiple telescopes observe the same target simultaneously ([Smith et al. 2020](#)). This mode is used for follow-ups of shallow transits detected by the NGTS survey, as well as for TESS targets ([Jenkins et al. 2020](#); [Armstrong et al. 2020](#)) and other exoplanets transiting bright stars ([Bryant et al. 2020](#)).

We observed a partial transit of NGTS-14Ab on the night of 2019 November 08 (the same event we observed with CHAT),

Table 2. Photometry of NGTS-14A.

BJD _{UTC} (−2450000)	Relative flux	σ_{flux}	Inst.
7562.688132	1.014176	0.006391	NGTS
7562.689019	0.993882	0.005278	NGTS
7562.690361	0.993867	0.005867	NGTS
7562.691707	0.997182	0.005817	NGTS
7562.693124	0.992255	0.005179	NGTS
7562.694540	1.001568	0.002645	NGTS
7562.695955	0.990161	0.004289	NGTS
7562.697372	0.991594	0.005725	NGTS
7562.698713	0.991647	0.005552	NGTS
7562.700052	0.992255	0.005312	NGTS

Notes. The full table is available at the CDS. Only a few lines are shown here for guidance on the format. It should be noted that the fitted offsets between datasets are not applied here, nor is our correction for contamination from NGTS-14B.

using eight of the NGTS telescopes. We obtained a total of 8790 exposures (around 1100 per camera), each with the usual NGTS exposure time (10 s) and cadence (13 s).

The NGTS follow-up data for NGTS-14A were reduced using a custom photometry pipeline. This pipeline uses the SEP Python library for both the source extraction and the aperture photometry ([Bertin & Arnouts 1996](#); [Barbary 2016](#)). We did not apply bias, dark, or flat-field image corrections during the image reduction as testing showed them to provide no improvement to the photometric precision achieved. We used *Gaia* ([Gaia Collaboration 2018](#)) to automatically identify comparison stars with a similar colour, brightness, and CCD position to those of NGTS-14A (see [Bryant et al. 2020](#), for more details on the photometric pipeline).

3.2.5. TESS

NGTS-14A falls in Sector 1 of the TESS survey, which was observed between 2018 July 25 and 2018 August 22, covering seven transits of NGTS-14Ab. We were able to extract a light curve from the full-frame images (FFIs) of Camera 1, CCD 2, which have a cadence of 30 min. To do this, we used a custom photometric aperture selected on the basis of a flux threshold and to minimise blending from other sources. A 15×15 pixel area was used for background estimation.

We ran the BLS algorithm on the TESS data to test if the planet could have been detected from the TESS data alone. A peak at around 3.5 d is the highest in the resulting periodogram, with a significance (following [Collier Cameron et al. 2006](#)) of 10.9. This suggests that an exhaustive search of light curves derived from the TESS FFIs could have revealed this system. However, the transit is much less evident in the TESS data compared with the NGTS data. This is primarily due to the fact that NGTS typically produces higher-precision photometry for stars with $T > 12.5$. The transit photometry from all the instruments listed above is presented in Table 2 and shown in Fig. 2.

3.3. High resolution spectroscopy

3.3.1. CORALIE

We observed NGTS-14A with the CORALIE spectrograph on the 1.2-m Euler-Swiss telescope at La Silla Observatory ([Queloz et al. 2001b](#)) between 2018 November 03 and December 04.

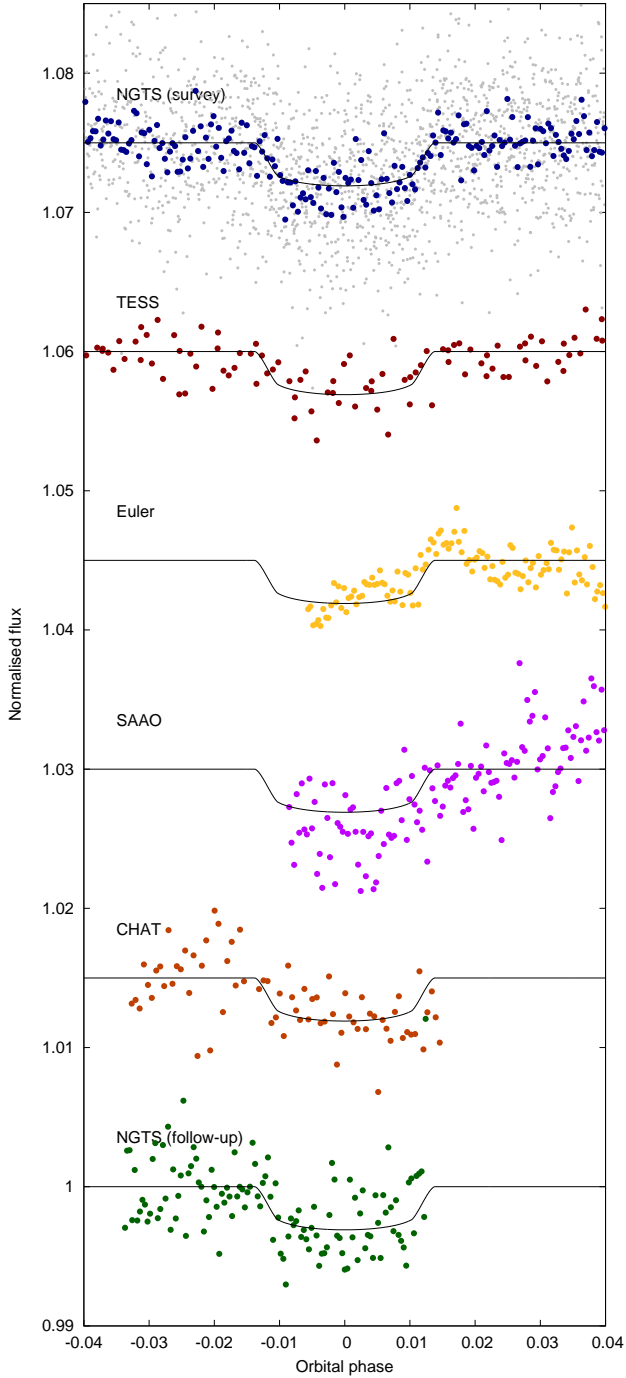


Fig. 2. Transit photometry of NGTS-14A from several instruments, offset vertically for clarity. *From top to bottom:* NGTS survey photometry (binned to two minutes in grey, binned to two minute equivalent in phase in blue); TESS (unbinned); Euler (binned to two minutes); SAAO (binned to two minutes); CHAT (unbinned); and single night NGTS multi-telescope observations (binned to two minutes). Our best fitting model is shown as a solid black line.

CORALIE has a resolving power of $R \sim 60\,000$ and is fed by a $2''$ on-sky science fibre. Radial velocity measurements were computed for each epoch by cross-correlating the spectra with a binary G2 mask (Pepe et al. 2002). The observations showed no significant RV variation within the uncertainties of $\sim 46\text{ m s}^{-1}$ and were used to screen NGTS-14A for possible scenarios of blended eclipsing binaries mimicking a planetary transit.

Table 3. Radial velocities for NGTS-14A.

BJD _{UTC} (−2450000)	RV (m s ^{−1})	RV err (m s ^{−1})	FWHM (m s ^{−1})	BIS (m s ^{−1})
8698.71245	30 272.51	4.38	6 147.32	8.36
8699.65656	30 294.53	5.40	6 139.47	5.61
8700.69210	30 299.43	4.63	6 153.15	−1.84
8717.70010	30 298.77	8.05	6 160.60	13.47
8718.60361	30 297.13	4.38	6 161.24	7.71
8719.73729	30 276.65	4.14	6 157.38	11.83
8721.65430	30 302.65	4.81	6 158.79	2.14
8722.60994	30 277.93	4.79	6 140.92	20.31
8723.58722	30 276.65	4.62	6 131.25	10.87
8724.53490	30 295.00	7.17	6 141.78	12.75
8724.80470	30 299.44	5.63	6 120.43	20.12
8725.56246	30 292.16	5.89	6 124.07	4.17
8725.74721	30 287.79	7.45	6 134.53	43.93
8730.60832	30 282.33	7.34	6 131.68	21.46
8746.58959	30 287.98	7.77	6 119.95	8.34

3.3.2. HARPS

We observed NGTS-14A using the HARPS spectrograph (Mayor et al. 2003) on ESO’s 3.6-m telescope at La Silla Observatory under programmes 0103.C-0719 and 0104.C-0588. A total of 15 measurements were made between 2019 August 03 and 2019 September 20.

We used the standard HARPS data reduction software to obtain RV measurements of NGTS-14A at each epoch. This was done via cross-correlation with a K5 binary mask. Bisector-span, full width at half maximum (FWHM), and other line-profile diagnostics were computed as well. Using an exposure time of 2700 s, we obtained typical error bars of $\sim 5\text{ m s}^{-1}$. The resulting RVs are listed in Table 3 and plotted in Fig. 3.

The HARPS science fibre has a $1''$ on-sky projection and thus does not include NGTS-14B. We co-added the 15 HARPS spectra while weighting each epoch by the inverse variance. Section 4.1 details the spectral analysis performed on the stacked spectrum.

4. Stellar characterisation

4.1. Spectral analysis

The HARPS spectra were co-added, and the resulting spectrum ($S/N \approx 49$) was analysed with the synthesis method (without the use of wavelets) outlined in Gill et al. (2018). The resulting parameters are $T_{*,\text{eff}} = 5200 \pm 85\text{ K}$, $[\text{Fe}/\text{H}] = 0.12 \pm 0.08$, $\log g_* = 4.2 \pm 0.1\text{ (cgs)}$, and $v \sin i_* = 1.2 \pm 0.5\text{ km s}^{-1}$.

4.2. SED fit with ARIADNE

We fit the spectral energy distribution (SED) of NGTS-14A using ARIADNE, a python tool written to fit catalogue photometry to different atmospheric model grids (Fig. 4). It hosts model grids for Phoenix v2 (Husser et al. 2013), BT-Settl, BT-Cond, BT-NextGen (Allard et al. 2012; Hauschildt et al. 1999), Castelli & Kurucz (2003), and Kurucz (1993), convolved with the following filter response functions: *UBVRI*; 2MASS *JHK_{rms}*; SDSS *ugriz*; WISE *W1* and *W2*; *Gaia G*, *RP*, and *BP*; Pan-STARRS *grizy_z*; Strömgren *uvby*; GALEX *NUV* and *FUV*; *TESS*; *Kepler*; and NGTS. Each synthetic SED is modelled by interpolating

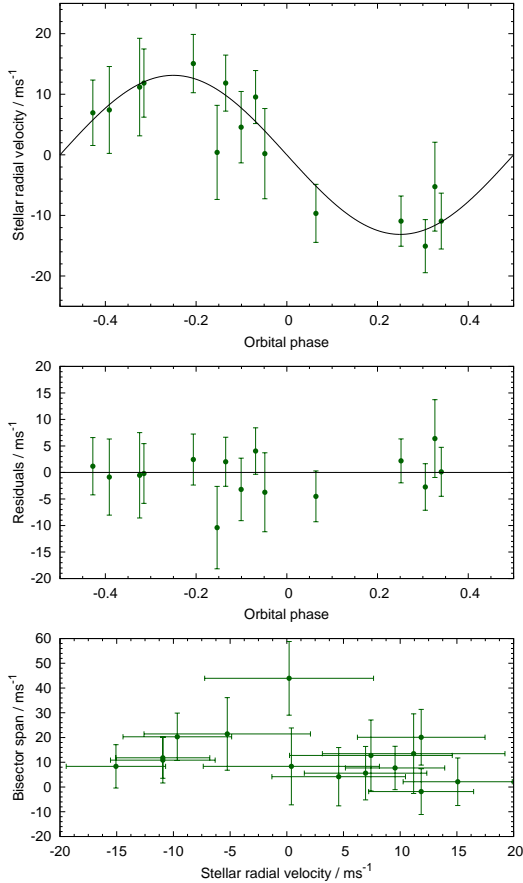


Fig. 3. Radial velocities of NGTS-14A from HARPS. *Upper panel:* RV as a function of orbital phase, with best fitting model shown as a solid black line. *Middle panel:* residuals to the best fitting model. *Lower panel:* bisector span of the stellar lines against RV. The uncertainties on the bisector spans are taken to be twice the uncertainty on the RVs.

grids in $T_{*,\text{eff}}-\log g_*-[\text{Fe}/\text{H}]$ space, with the remaining parameters being distance, radius, and extinction in the V -band as well as an individual excess noise for each photometry in order to account for underestimated uncertainties. The priors for $T_{*,\text{eff}}$, $\log g_*$, and $[\text{Fe}/\text{H}]$ were taken from the spectral analysis determined values, and we took the *Gaia* DR2 reported values for radius and distance; we note that we inflated the radius reported error to account for modelling errors, and that we applied the [Stassun & Torres \(2018\)](#) correction to the parallax. We limited the A_V to the maximum line-of-sight taken from the Galactic dust map of [Schlegel et al. \(1998\)](#), as re-calibrated by [Schlafly & Finkbeiner \(2011\)](#) and each excess noise parameter has a zero mean normal distribution as their priors, with a variance equal to five times the size of the reported uncertainty. ARIADNE uses *dynesty*'s nested sampler for parameter estimation and for calculating the Bayesian evidence for each model ([Speagle 2020](#)). The final step in ARIADNE's algorithm is calculating the weighted average of each parameter using the relative probabilities of each model as weights. A detailed explanation of the fitting procedure, accuracy, and precision of ARIADNE is available in [Vines & Jenkins \(2020\)](#). The resulting stellar parameters are listed in Table 4.

4.3. TIC

The TESS Input Catalog (TIC) ([Stassun et al. 2019](#)) lists the following parameters for NGTS-14A, based on the *Gaia* DR2 A183, page 6 of 11

Table 4. Stellar parameters.

Parameter	Value	Source
$T_{*,\text{eff}}/\text{K}$	5187 ± 11	ARIADNE
$\log g_*$ (cgs)	4.20 ± 0.04	ARIADNE
$v \sin i_*/\text{km s}^{-1}$	1.2 ± 0.5	HARPS spectrum
$[\text{Fe}/\text{H}]$	0.10 ± 0.03	ARIADNE
R_*/R_\odot	0.842 ± 0.006	ARIADNE
M_*/M_\odot	0.898 ± 0.035	ARIADNE
Age/Gyr	$5.9^{+3.0}_{-3.4}$	ARIADNE

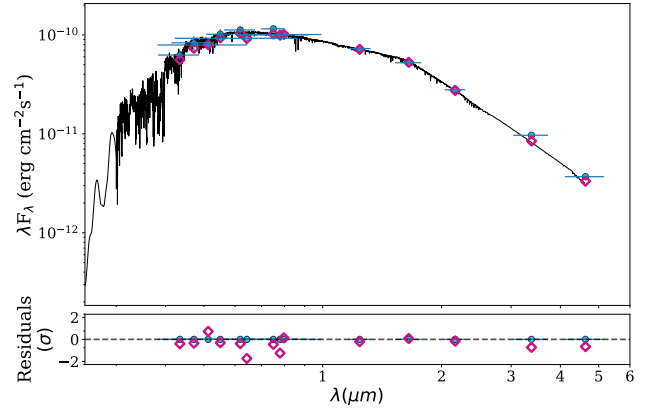


Fig. 4. Spectral energy distribution (SED) of NGTS-14A. Catalogue photometric measurements (Table 1) are shown as blue circles, with the horizontal error bars indicating the extent of each bandpass. A model SED from [Castelli & Kurucz \(2003\)](#) is shown as a solid black line, with magenta squares indicating the model flux integrated over each bandpass.

([Gaia Collaboration 2018](#)) observations: $R_* = 0.856 \pm 0.049 R_\odot$ and $T_{*,\text{eff}} = 5222 \pm 128 \text{ K}$. We note that our adopted values are in good agreement with these TIC values.

4.4. Stellar rotation

We searched the NGTS survey light curve for periodic signals, using both a Lomb-Scargle periodogram and a generalised autocorrelation (G-ACF) method ([Gillen et al. 2020](#)). Both methods revealed a signal with a period of approximately 10 d to be the most prominent; however, given the small amplitude of the putative signal ($\leq 1 \text{ mmag}$), this is not a robust detection.

From the $v \sin i_*$ derived from the HARPS spectra ($1.2 \pm 0.5 \text{ km s}^{-1}$) and the stellar radius, we calculated an upper limit to the stellar rotation period, $P_{*,\text{rot}} \leq 35.5 \pm 14.8 \text{ d}$. This value corresponds to the case where the stellar spin and planet rotation axes are aligned.

It is unclear if the 10-d signal is related to rotation since that would imply a faster rotating star than suggested by the $v \sin i_*$ and would be indicative of a star significantly younger (c. 700 Myr; [Rebull et al. 2017](#); [Douglas et al. 2017](#)) than what our SED analysis implies (Sect. 4.2). At an age of less than 1 Gyr, K0 stars typically exhibit a photometric rotational modulation of at least a few millimagnitudes, which would be readily detectable in the NGTS data.

5. Joint fit to photometry and RVs

We performed a joint fit to the photometry and RVs using the Transit and Light Curve Modeller (TLCM; [Csizmadia 2020](#)).

In order to reduce the large number of data points in the NGTS survey photometry, and thus increase modelling speed, we modelled only those nights of NGTS data where a transit occurred, and we binned the remaining light curve to a cadence of 120 s. This resulted in a total of 2404 NGTS survey data points. Similarly, the NGTS multi-telescope data were binned to a single light curve with a cadence of 120 s. We excluded TESS data taken far from transit, only modelling those data with an orbital phase between -0.1 and 0.1 . The CHAT, SAAO, and Euler light curves were modelled unbinned and in their entirety.

5.1. Contaminating flux from NGTS-14B

In all photometric datasets, except that from the SAAO 1-m, NGTS-14B (Sect. 2) is well within the photometric aperture used to extract the target flux from the images. To account for this contamination, we calculated the flux ratio of the two components of NGTS-14 and corrected the affected datasets accordingly. We find that NGTS-14B contributes around two per cent of the observed flux and that, in the absence of any correction, our value of R_p/R_* is biased by around 2σ .

5.2. Stellar limb darkening

The signal-to-noise ratio of our photometry is not sufficiently high to precisely constrain the limb-darkening coefficients in each bandpass in which we observed NGTS-14A. The bandpasses used do not span a particularly large range of wavelengths; rather, they are fairly similar to one another. We calculated theoretically expected quadratic limb-darkening coefficients for each band using the Limb Darkening Toolkit (LDTk) from Parviainen & Aigrain (2015), which relies on the stellar models in Husser et al. (2013). The difference between the coefficients for the different bandpasses is insignificant, much smaller than the uncertainties on the coefficients we measured for each light curve individually. Furthermore, we find that our derived system parameters are insensitive to our choice of limb-darkening parameters within this range. We therefore opted to fit for a single pair of limb-darkening coefficients that is common to all observed bandpasses. In the TLCM, this is done with the parameters $u_+ = u_a + u_b$ and $u_- = u_a - u_b$, where u_a and u_b are the commonly used quadratic coefficients.

5.3. Orbital eccentricity

We also tried fitting for an eccentric orbit via the additional parameters $\sqrt{e} \sin(\omega)$ and $\sqrt{e} \cos(\omega)$, where e is the orbital eccentricity and ω the argument of periastron. Our best fitting values are $\sqrt{e} \sin(\omega) = 0.07 \pm 0.27$ and $\sqrt{e} \cos(\omega) = -0.05 \pm 0.20$, resulting in $e = 0.0074 \pm 0.0428$ and $\omega = -54 \pm 151$ degrees. The three-sigma upper limit to the eccentricity is 0.11. The very modest improvement in χ^2 of less than 0.4 does not compensate for the much larger Bayesian penalty on having two additional model parameters. This results in a significantly lower Bayesian information criterion (BIC) for the circular orbital model ($\Delta \text{BIC}_{\text{circ-ecc}} = -5.05$). We therefore rejected the eccentric model and adopted $e = 0$.

5.4. Additional trend in RVs

We also tried fitting for a radial acceleration, $\dot{\gamma}$, of NGTS-14A. The presence of such a trend in the RVs is usually indicative of an additional body in the system (e.g. Smith et al. 2017). We obtained a best fitting value of $\dot{\gamma} = -9_{-17}^{+21} \text{ m s}^{-1} \text{ yr}^{-1}$, suggesting

that no significant radial acceleration is detected. This was confirmed by a BIC analysis; the simpler model with no acceleration has a smaller BIC value (by 1.2) and is hence preferred.

5.5. Bisector spans

We observe no evidence for a correlation between either time and bisector span or bisector span and RV (Fig. 3). A correlation can indicate that the apparent planetary signal is caused by a blended eclipsing binary system or by stellar activity (Queloz et al. 2001a). Furthermore, we see no correlation between RV and the FWHM of the line profile.

Our joint fits to the photometry and RVs are shown in Figs. 2 and 3, respectively. The resulting system parameters are listed in Table 5.

6. Discussion

6.1. NGTS-14Ab in the Neptunian desert

NGTS-14Ab joins a growing number of planets that reside in the Neptunian desert, a sparsely populated region of parameter space between the hot Jupiters and the super Earths in the radius-period plane (Fig. 5). NGTS-14Ab lies within both the desert as defined by Mazeh et al. (2016) and the smaller region identified by Szabó & Kálmán (2019), who, along with Eigmüller et al. (2019), have recently investigated the boundaries of the Neptunian desert as a function of host star spectral type.

Owen & Lai (2018) explain the lower boundary of the desert as a consequence of photoevaporation – a process that is more efficient at reducing the size of close-in planets. Furthermore, they suggest that the upper boundary of the desert is a result of the fact that only the highest-mass planets can be tidally circularised in the closest orbits after high-eccentricity migration. NGTS-14Ab lies among the lower boundaries of the desert computed by Owen & Lai (2018), which are dependent upon metallicity and core mass. Comparing NGTS-14Ab to their simulations (which ran for 5 Gy, similar to the age of the system) suggests that NGTS-14Ab has a core mass of close to $10 M_{\oplus}$ and that any additional envelope accreted by the planet during its formation would have by now been lost to photoevaporation.

We used the neural network model of planetary interiors developed by Baumeister et al. (2020) to predict the internal structure of NGTS-14Ab (Fig. 6), using the planetary mass and radius (Table 5) as model inputs. Although internal structure is notoriously degenerate with mass and radius, this model suggests that NGTS-14Ab has a significant gaseous envelope. The models of Howe et al. (2014) suggest that an H_2 -He envelope constituting approximately half of the planet’s radius would contribute five to ten per cent of the planet’s mass, for a core mass of $10 M_{\oplus}$. In other words, there is broad compatibility between the models of Baumeister et al. (2020) (Fig. 6) and the model of Zeng et al. (2019) that has a five per cent (by mass) hydrogen-rich envelope (Fig. 7, red curve).

In Fig. 7, we compare NGTS-14Ab to the other planets that inhabit ‘Region A’ of Szabó & Kálmán (2019), that is, those planets having radii between 0.28 and $0.63 R_{\text{Jup}}$. Planets orbiting closer to their stars than NGTS-14Ab does, such as NGTS-4 b (West et al. 2019) and TOI-132 b (Díaz et al. 2020), tend to be denser because they have undergone evaporation and lost much or all of their primary, hydrogen-dominated atmospheres. The most extreme example of this is the recently discovered TOI-849 b (Armstrong et al. 2020), thought to be the remnant core of a giant planet. LTT 9779 b (Jenkins et al. 2020),

Table 5. Parameters from light curve and RV data analysis.

Parameter	Value	Unit
TLCM fitted parameters		
Orbital period P_{orb}	3.5357173 ± 0.0000069	d
Transit epoch T_0	7502.5545 ± 0.0020	BJD _{TDB} – 2450000
Scaled semi-major axis a/R_*	$10.3^{+2.3}_{-2.6}$	
Radius ratio R_p/R_*	$0.0530^{+0.0038}_{-0.0033}$	
Transit impact parameter b	$0.59^{+0.23}_{-0.38}$	
Limb-darkening coefficient u_+	0.65 ± 0.19	
Limb-darkening coefficient u_-	0.30 ± 0.21	
Radial velocity semi amplitude K	13.2 ± 1.7	m s ⁻¹
Systemic radial velocity γ	30.2876 ± 0.0013	km s ⁻¹
Derived parameters:		
Eccentricity e	0.0	(fixed, see Sect. 5.3)
Semi-major axis a	0.0403 ± 0.0071	au
Orbital inclination angle i	86.7 ± 1.7	deg
Transit Duration T_{14}	$2.24^{+0.08}_{-0.06}$	h
Planet mass M_p	0.092 ± 0.012	M_{Jup}
Planet radius R_p	0.444 ± 0.030	R_{Jup}
Planet mean density	1395 ± 333	kg m ⁻³
Planet surface gravity $\log g_p$	3.08 ± 0.08	(cgs)
Planet equilibrium temperature ^(†) $T_{p,A=0}$	1143 ± 139	K

Notes. ^(†) Assuming zero albedo, and isotropic heat redistribution.

on the other hand, remains an intriguing exception – how it has apparently retained its hydrogen-rich envelope is a mystery. NGTS-14Ab appears to be just far enough from its star that it is able to maintain a significant atmosphere, resulting in a density similar to those of Uranus and Neptune.

6.2. Stellar companion

Motivated by the apparent stellar companion to NGTS-14A (Sect. 2) and NGTS-14Ab’s position in the Neptunian desert (as defined by Mazeh et al. 2016), we conducted a search for stellar companions to other planet host stars in and around the desert. The presence of a long-period companion may influence the evolution of a planetary system, for instance by driving high-eccentricity migration (Wu & Murray 2003).

We used the *Gaia* DR2 catalogue (Gaia Collaboration 2018) to search for companions to stars that are listed in the NASA Exoplanet Archive⁴ as hosting planets with orbital periods of less than 50 per cent. We then sub-divided the sample into planets lying above, in, or below the Neptunian desert (as defined in the mass-period plane in Mazeh et al. 2016). This resulted in 73 systems in the desert, 339 systems above the desert, and 55 systems (70 planets) below the desert.

We then queried *Gaia* DR2, via a cone search centred on each object, using the astroquery package (Ginsburg et al. 2019). The radius of the search was chosen individually for each object so that it corresponded to a separation of 10 000 au. We then applied the same technique as used in Sect. 2 to search for nearby objects whose parallaxes and proper motions match the planet

host star within $n\sigma$. For $n = 3$, we identified possible companions to 62 host stars (18.3%) from above the desert, ten (13.7%) in the desert, and three (5.5%) below it. Combining the results for above and below the desert, we find potential companions to 16.5% of host stars outside the desert, which is statistically indistinguishable from the proportion inside the desert. These results are summarised in Table 6.

To extend our binarity analysis to companions too close to be resolved as individual objects in *Gaia* DR2, we used the re-normalised unit weight error (RUWE) on the *Gaia* DR2 astrometric solutions (Lindgren et al. 2018). A previous analysis conducted using the RUWE statistic has suggested that there is tentative evidence for increased binarity among hot Jupiter host stars (Belokurov et al. 2020).

We adopted the threshold of $\text{RUWE} = 1.4$ suggested by the *Gaia* team for distinguishing between well-behaved solutions and those where an unseen additional body may impact the astrometry⁵. In Table 6, we report the number of systems for which the RUWE statistic is greater than 1.4. We fail to find a significant difference between the RUWE distributions for objects inside and outside the Neptunian desert. There is, however, a hint of fewer companions below the desert, with no large RUWE values in this population.

Finally, we attempted to compare the three populations of exoplanet-hosting stars with their non-exoplanet host counterparts. To do this, for each exoplanet host star, we searched *Gaia* DR2 for other nearby stars with similar properties. Specifically, we required that the G -band magnitude be within 0.25, the $G_{\text{BP}} - G_{\text{RP}}$ colour within 15 per cent, and the parallax within a factor of two (to exclude giant stars). Where multiple stars were

⁴ <https://exoplanetarchive.ipac.caltech.edu/>, accessed 2020 June 17.

⁵ Technical note *Gaia*-C3-TN-LU-LL-124-01 http://www.rssd.esa.int/doc_fetch.php?id=3757412

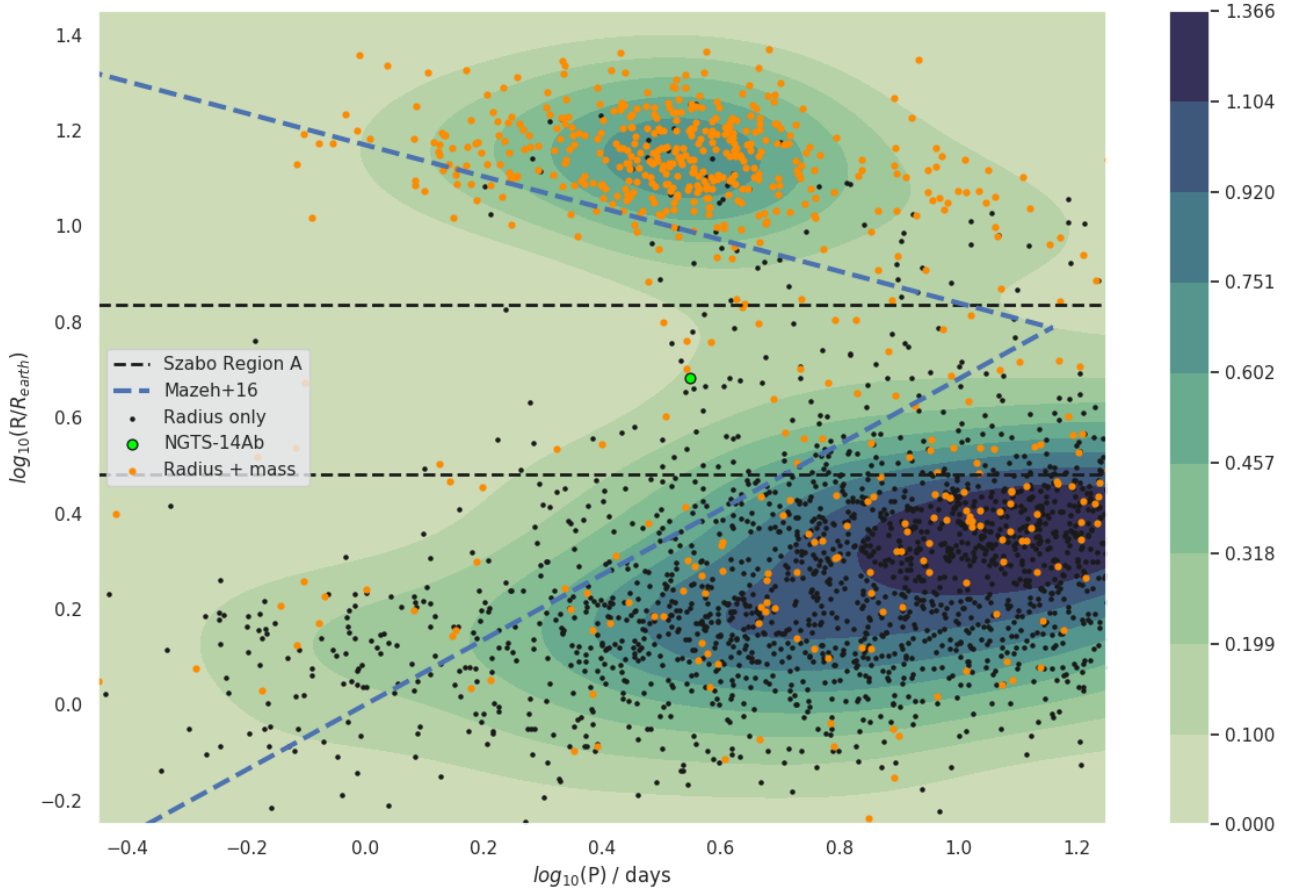


Fig. 5. NGTS-14Ab (light green point) within the Neptunian desert, the boundary of which (as defined by Mazeh et al. 2016) is indicated with dashed blue lines. The dashed black lines indicate the region of interest identified by Szabó & Kálmán (2019). The parameters of other planets come from the NASA Exoplanet Archive, and the colour scale indicates the number of planets per grid element. The plot comprises 200×200 elements, uniformly spaced in $\log_{10} P$ and $\log_{10} R$.

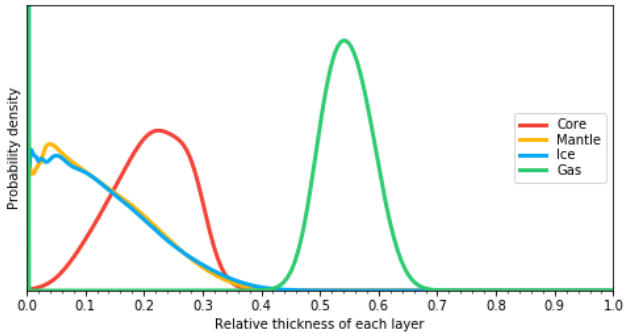


Fig. 6. Possible internal structure for NGTS-14Ab, the result of the neural network model of Baumeister et al. (2020). Shown are the predictions of the relative interior layer thicknesses, using our derived planetary mass and radius as inputs. The coloured lines show the combined Gaussian mixture prediction of the model, with the area under each curve normalised to unity.

found to match these criteria, we selected one at random. We then performed the same analysis on these non-exoplanet host stars as on the hosts; the results are reported in the lower part of Table 6.

We see fewer potential long-period companions with matching parallaxes and proper motions among the non-host stars, suggesting that the presence of a long-period companion increases

the probability of a star hosting an exoplanet in or above the desert. Non-well-behaved ($\text{RUWE} > 1.4$) astrometric solutions are more likely to occur around stars not known to host an exoplanet, perhaps indicating that short-period binaries are more common in this population. We note, however, that selection effects may play a role here, in that the short-period binarity of an exoplanet candidate host star may complicate both photometric and spectroscopic follow-up, and hence the confirmation of exoplanets orbiting stars with close binary companions.

Although this binarity analysis is inconclusive, future *Gaia* data releases will include the identification of further gravitationally bound companions to exoplanet host stars. This may allow any trends with planet parameters (such as membership of the Neptunian desert) to be elucidated.

7. Conclusions

We have presented the discovery of the NGTS-14 system, which consists of an early K-type dwarf star, NGTS-14A, with a long-period companion, NGTS-14B, which is likely to be a mid-M dwarf. The primary star is orbited by a transiting exoplanet, NGTS-14Ab, which is slightly larger and more massive than Neptune. The planet's orbital period of just over 3.5 days places it in the Neptunian desert, a sparsely populated region of parameter space. NGTS-14Ab has a density that suggests that it has retained some of its primordial atmosphere.

Table 6. Potential companions to planetary host stars, based on analysis of *Gaia* DR2 data.

Subset	No. of systems	Plx & PM matches		RUWE > 1.4	
		No.	%	No.	%
Exoplanet host stars					
Desert	73	10	13.7	4	5.5
Above desert	339	62	18.3	18	5.3
Below desert	55	3	5.5	0	0.0
Above + below	394	65	16.5	18	4.6
Sum of all host stars	467	75	15.6	22	4.6
Analogous non-host stars					
Desert	73	1	1.4	11	15.1
Above desert	339	27	8.0	49	14.5
Below desert	55	5	9.1	14	25.5
Sum of all non-host stars	467	33	7.1	74	15.8

Notes. ‘Plx & PM matches’ refers to potential long-period companions identified by their matching parallaxes and proper motions. ‘RUWE > 1.4’ refers to stars whose astrometric fits exhibit excess noise, potentially indicating the presence of a binary companion.

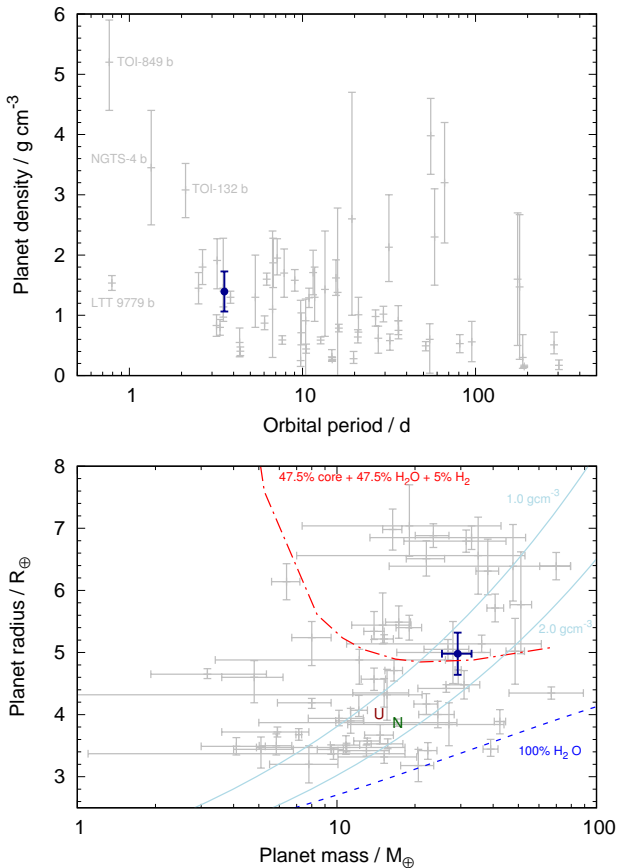


Fig. 7. NGTS-14Ab compared to other planets within the Neptunian desert, as defined by Szabó & Kálmán (2019) (their ‘Region A’ is the area between the dashed black lines in Fig. 5). Planetary data are taken from the NASA Exoplanet Archive. NGTS-14Ab is denoted by a dark blue point in both panels. *Upper panel:* planet density versus orbital period. Several planets discussed in the text are labelled with their names. *Lower panel:* planet radius versus mass. The Solar System ice giants are indicated with their initial letters, and lines of constant density (1.0 and 2.0 g cm⁻³) are shown with solid pale blue lines. Two models from Zeng et al. (2019), corresponding to compositions of pure water (dashed blue line) and an Earth-like rocky core with an equal mass of water and five per cent hydrogen (dash-dotted red line), are also shown.

Acknowledgements. This work uses data collected under the NGTS project at the ESO La Silla Paranal Observatory. The NGTS facility is operated by the consortium institutes with support from the UK Science and Technology Facilities Council (STFC) under projects ST/M001962/1 and ST/S002642/1. This research made use of Astropy⁶, a community-developed core Python package for Astronomy (Astropy Collaboration 2013, 2018). This work has made use of data from the European Space Agency (ESA) mission *Gaia* (<https://www.cosmos.esa.int/gaia>), processed by the *Gaia* Data Processing and Analysis Consortium (DPAC, <https://www.cosmos.esa.int/web/gaia/dpac/consortium>). Funding for the DPAC has been provided by national institutions, in particular the institutions participating in the *Gaia* Multilateral Agreement. This research has made use of the NASA Exoplanet Archive, which is operated by the California Institute of Technology, under contract with the National Aeronautics and Space Administration under the Exoplanet Exploration Program. This publication makes use of data products from the Wide-field Infrared Survey Explorer, which is a joint project of the University of California, Los Angeles, and the Jet Propulsion Laboratory/California Institute of Technology, funded by the National Aeronautics and Space Administration. This study is based on observations collected at the European Southern Observatory under ESO programmes 0103.C-0719 and 0104.C-0588. We thank the Swiss National Science Foundation (SNSF) and the Geneva University for their continuous support to our planet search programs. This work has been in particular carried out in the frame of the National Centre for Competence in Research PlanetS supported by the Swiss National Science Foundation (SNSF). This publication makes use of The Data & Analysis Center for Exoplanets (DACE), which is a facility based at the University of Geneva (CH) dedicated to extrasolar planets data visualisation, exchange and analysis. DACE is a platform of the Swiss National Centre of Competence in Research (NCCR) PlanetS, federating the Swiss expertise in Exoplanet research. The DACE platform is available at <https://dace.unige.ch>. M.N.G. acknowledges support from MIT’s Kavli Institute as a Juan Carlos Torres Fellow. Contributions by authors from the University of Warwick were supported by STFC consolidated grants ST/P000495/1 and ST/T000406/1. D.J.A. acknowledges support from the STFC via an Ernest Rutherford Fellowship (ST/R00384X/1). E.G. gratefully acknowledges support from the David and Claudia Harding Foundation in the form of a Winton Exoplanet Fellowship. Ph.E., A.C., and H.R. acknowledge the support of the DFG priority program SPP 1992 “Exploring the Diversity of Extrasolar Planets” (RA 714/13-1). R.B. acknowledges support from FONDECYT Post-doctoral Fellowship Project 3180246, and from the Millennium Institute of Astrophysics (MAS). Finally, we acknowledge our anonymous referee, whose comments helped to improve the quality of this manuscript.

References

- Allard, F., Homeier, D., & Freytag, B. 2012, *Philos. Trans. R. Soc. A Math., Phys. Eng. Sci.*, 370, 2765
 Armstrong, D. J., Lopez, T. A., Adibekyan, V., et al. 2020, *Nature*, 583, 39
 Astropy Collaboration (Robitaille, T. P., et al.) 2013, *A&A*, 558, A33

⁶ <http://www.astropy.org>

- Astropy Collaboration (Price-Whelan, A. M., et al.) 2018, *AJ*, 156, 123
- Bakos, G. Á., Lázár, J., Papp, I., Sári, P., & Green, E. M. 2002, *PASP*, 114, 974
- Barbary, K. 2016, *J. Open Source Softw.*, 58
- Baumeister, P., Padovan, S., Tosi, N., et al. 2020, *ApJ*, 889, 42
- Belokurov, V., Penoyre, Z., Oh, S., et al. 2020, *MNRAS*, 496, 1922
- Bertin, E., & Arnouts, S. 1996, *A&AS*, 117, 393
- Borucki, W. J., Koch, D., Basri, G., et al. 2010, *Science*, 327, 977
- Bryant, E. M., Bayliss, D., McCormac, J., et al. 2020, *MNRAS*, 494, 5872
- Castelli, F., & Kurucz, R. L. 2003, *Modelling of Stellar Atmospheres*, eds. N. Piskunov, W. W. Weiss, & D. F. Gray (Cambridge: Cambridge University Press), 210, A20
- Chaushev, A., Raynard, L., Goad, M. R., et al. 2019, *MNRAS*, 488, 5232
- Collier Cameron, A., Pollacco, D., Street, R. A., et al. 2006, *MNRAS*, 373, 799
- Coppejans, R., Gulbis, A. A. S., Kotze, M. M., et al. 2013, *PASP*, 125, 976
- Csizmadia, S. 2020, *MNRAS*, 496, 4442
- Cutri, R. M. et al. 2014, VizieR Online Data Catalog: II/328
- Díaz, M. R., Jenkins, J. S., Gandolfi, D., et al. 2020, *MNRAS*, 493, 973
- Douglas, S. T., Agüeros, M. A., Covey, K. R., & Kraus, A. 2017, *ApJ*, 842, 83
- Eigmüller, P., Chaushev, A., Gillen, E., et al. 2019, *A&A*, 625, A142
- Espinoza, N., Hartman, J. D., Bakos, G. Á., et al. 2019, *AJ*, 158, 63
- Gaia Collaboration (Prusti, T., et al.) 2016, *A&A*, 595, A1
- Gaia Collaboration (Brown, A. G. A., et al.) 2018, *A&A*, 616, A1
- Gill, S., Maxted, P. F. L., & Smalley, B. 2018, *A&A*, 612, A111
- Gillen, E., Briegal, J. T., Hodgkin, S. T., et al. 2020, *MNRAS*, 492, 1008
- Ginsburg, A., Sipőcz, B. M., Brasseur, C. E., et al. 2019, *AJ*, 157, 98
- Günther, M. N., Queloz, D., Gillen, E., et al. 2017, *MNRAS*, 472, 295
- Hartman, J. D., Bakos, G. Á., Bayliss, D., et al. 2019, *AJ*, 157, 55
- Hauschildt, P. H., Allard, F., & Baron, E. 1999, *ApJ*, 512, 377
- Henden, A. A., Templeton, M., Terrell, D., et al. 2016, VizieR Online Data Catalog: II/336
- Howe, A. R., Burrows, A., & Verne, W. 2014, *ApJ*, 787, 173
- Howell, S. B., Sobeck, C., Haas, M., et al. 2014, *PASP*, 126, 398
- Husser, T.-O., Wende-von Berg, S., Dreizler, S., et al. 2013, *A&A*, 553, A6
- Jenkins, J. S., Díaz, M. R., Kurtovic, N. T., et al. 2020, *Nat. Astron.*, 4, 1148
- Jiang, Y.-F., & Tremaine, S. 2010, *MNRAS*, 401, 977
- Jordán, A., Brahm, R., Espinoza, N., et al. 2019, *AJ*, 157, 100
- Kovács, G., Zucker, S., & Mazeh, T. 2002, *A&A*, 391, 369
- Kurucz, R. L. 1993, VizieR Online Data Catalog: VI/039
- Lindgren, L., Hernández, J., Bombrun, A., et al. 2018, *A&A*, 616, A2
- Mayor, M., Pepe, F., Queloz, D., et al. 2003, *The Messenger*, 114, 20
- Mazeh, T., Holczer, T., & Faigler, S. 2016, *A&A*, 589, A75
- McCormac, J., Pollacco, D., Skillen, I., et al. 2013, *PASP*, 125, 548
- Owen, J. E., & Lai, D. 2018, *MNRAS*, 479, 5012
- Parviainen, H., & Aigrain, S. 2015, *MNRAS*, 453, 3821
- Pecaut, M. J., & Mamajek, E. E. 2013, *ApJS*, 208, 9
- Pepe, F., Mayor, M., Rupprecht, G., et al. 2002, *The Messenger*, 110, 9
- Pollacco, D. L., Skillen, I., Cameron, A. C., et al. 2006, *PASP*, 118, 1407
- Queloz, D., Henry, G. W., Sivan, J. P., et al. 2001a, *A&A*, 379, 279
- Queloz, D., Mayor, M., Udry, S., et al. 2001b, *The Messenger*, 105, 1
- Rebull, L. M., Stauffer, J. R., Hillenbrand, L. A., et al. 2017, *ApJ*, 839, 92
- Ricker, G. R., Winn, J. N., Vanderspek, R., et al. 2015, *J. Astron. Telesc. Instrum. Syst.*, 1, 014003
- Schlafly, E. F., & Finkbeiner, D. P. 2011, *ApJ*, 737, 103
- Schlegel, D. J., Finkbeiner, D. P., & Davis, M. 1998, *ApJ*, 500, 525
- Sestovic, M., Demory, B.-O., & Queloz, D. 2018, *A&A*, 616, A76
- Sing, D. K., Fortney, J. J., Nikolov, N., et al. 2016, *Nature*, 529, 59
- Skrutskie, M. F., Cutri, R. M., Stiening, R., et al. 2006, *AJ*, 131, 1163
- Smith, A. M. S., Gandolfi, D., Barragán, O., et al. 2017, *MNRAS*, 464, 2708
- Smith, A. M. S., Eigmüller, P., Gurumoorthy, R., et al. 2020, *Astron. Nachr.*, 341, 273
- Speagle, J. S. 2020, *MNRAS*, 493, 3132
- Stassun, K. G., & Torres, G. 2018, *ApJ*, 862, 61
- Stassun, K. G., Oelkers, R. J., Paegert, M., et al. 2019, *AJ*, 158, 138
- Szabó, G. M., & Kiss, L. L. 2011, *ApJ*, 727, L44
- Szabó, G. M., & Kálmán, S. 2019, *MNRAS*, 485, L116
- Tamuz, O., Mazeh, T., & Zucker, S. 2005, *MNRAS*, 356, 1466
- Thorngren, D. P., & Fortney, J. J. 2018, *AJ*, 155, 214
- Vines, J. I., & Jenkins, J. S. 2020, in prep
- West, R. G., Gillen, E., Bayliss, D., et al. 2019, *MNRAS*, 486, 5094
- Wheatley, P. J., West, R. G., Goad, M. R., et al. 2018, *MNRAS*, 475, 4476
- Wu, Y., & Murray, N. 2003, *ApJ*, 589, 605
- Zeng, L., Jacobsen, S. B., Sasselov, D. D., et al. 2019, *Proc. Natl. Acad. Sci.*, 116, 9723